

# Unveiling Direct Electrochemical Oxidation of Methane at the Ceria/Gas Interface

Yoonseok Choi, Hyunwoo Ha, Jinwook Kim, Han Gil Seo, Hyuk Choi, Beomgyun Jeong, JeongDo Yoo, Ethan J. Crumlin, Graeme Henkelman, Hyun You Kim,\* and WooChul Jung\*

Solid oxide fuel cells (SOFCs) stand out in sustainable energy systems for their unique ability to efficiently utilize hydrocarbon fuels, particularly those from carbon-neutral sources.  $\text{CeO}_{2-\delta}$  (ceria) based oxides embedded in SOFCs are recognized for their critical role in managing hydrocarbon activation and carbon coking. However, even for the simplest hydrocarbon molecule,  $\text{CH}_4$ , the mechanism of electrochemical oxidation at the ceria/gas interface is not well understood and the capability of ceria to electrochemically oxidize methane remains a topic of debate. This lack of clarity stems from the intricate design of standard metal/oxide composite electrodes and the complex nature of electrode reactions involving multiple chemical and electrochemical steps. This study presents a Sm-doped ceria thin-film model cell that selectively monitors  $\text{CH}_4$  direct-electro-oxidation on the ceria surface. Using impedance spectroscopy, operando X-ray photoelectron spectroscopy, and density functional theory, it is unveiled that ceria surfaces facilitate C–H bond cleavage and that  $\text{H}_2\text{O}$  formation is key in determining the overall reaction rate at the electrode. These insights effectively address the longstanding debate regarding the direct utilization of  $\text{CH}_4$  in SOFCs. Moreover, these findings pave the way for an optimized electrode design strategy, essential for developing high-performance, environmentally sustainable fuel cells.

cells that can convert the chemical energy of fuels directly into electricity beyond the Carnot-cycle limit in applications such as transportation or stationary combined heating and power systems.<sup>[1,2]</sup> Most fuel cells require high-purity hydrogen as fuel. However, because current hydrogen production largely relies on reforming natural gas and the related delivery/storage infrastructure is still evolving, their near-term realization of both efficiency and cost competitiveness remains challenging.<sup>[3]</sup> In this context, solid oxide fuel cells (SOFCs) have received considerable attention due to their ability to operate directly with various hydrocarbons, in part because of their high operation ( $\geq 650$  °C), eliminating the need for additional reforming processes.<sup>[4]</sup> This is particularly relevant given that those are the main components of various carbon-neutral fuels such as biofuels and e-fuels, enhancing the role of SOFCs as a carbon-free power generation. Since Steele's pioneering studies in the early 1990s<sup>[5]</sup> and subsequent successful demonstrations by Barnett and Gorte in

1999 and 2000, respectively, the feasibility of SOFCs operating via the direct injection of hydrocarbon fuels, especially  $\text{CH}_4$ , has been established, and many related studies have since been reported.<sup>[6]</sup> Despite these efforts, however, poor electrode

## 1. Introduction

The growing need to improve energy efficiency along with reduced  $\text{CO}_2$  emission levels motivates the development of fuel

Y. Choi  
High Temperature Electrolysis Laboratory  
Korea Institute of Energy Research (KIER)  
Daejeon 34101, Republic of Korea

H. Ha, G. Henkelman  
Department of Chemistry  
The University of Texas at Austin  
Austin, TX 78712, United States

J. Kim, J. Yoo  
Department of Materials Science and Engineering  
Korea Advanced Institute of Science and Technology (KAIST)  
Daejeon 34129, Republic of Korea

H. G. Seo  
Department of Materials Science and Engineering  
Dankook University  
Chungnam 31116, Republic of Korea

 The ORCID identification number(s) for the author(s) of this article can be found under <https://doi.org/10.1002/adma.202403626>

DOI: 10.1002/adma.202403626

H. Choi, H. Y. Kim  
Department of Materials Science and Engineering  
Chungnam National University  
Daejeon 34134, Republic of Korea  
E-mail: [kimhy@cnu.ac.kr](mailto:kimhy@cnu.ac.kr)

B. Jeong  
Research Center for Materials Analysis  
Korea Basic Science Institute (KBSI)  
Daejeon 34133, Republic of Korea

E. J. Crumlin  
Advanced Light Sources  
Lawrence Berkeley National Laboratory (LBNL)  
Berkeley, CA 94720, USA

W. Jung  
Department of Materials Science and Engineering  
Research Institute of Advanced Materials  
Seoul National University (SNU)  
Seoul 08826, Republic of Korea  
E-mail: [wjung@snu.ac.kr](mailto:wjung@snu.ac.kr)

performance and short lifetimes continue to limit the commercialization of CH<sub>4</sub>-fed SOFC systems without an external reformer.<sup>[7]</sup>

Ceria (CeO<sub>2</sub>) has long been recognized as a critical material in using CH<sub>4</sub> as a fuel.<sup>[7a]</sup> Many successful instances of direct-methane SOFCs have been reported with metal/oxide composite anodes, including ceria as the main component. These successes arose due to a high resistance to carbon deposition and an excellent reactivity toward hydrocarbon oxidation when using this material, presumably stemming from its inherent ability to store and release oxygen. Ceria also transports oxygen ions more rapidly than the state-of-the-art solid electrolyte, yttria-stabilized zirconia (YSZ), yet retains an electron conductivity that easily exceeds that of oxygen ions in a reducing atmosphere.<sup>[8]</sup> Accordingly, the dominant electro-catalytic sites can be extended to ceria/gas interfaces beyond the metal/oxide/gas three-phase boundaries (3PBs).<sup>[9]</sup> Given these features, it has been argued that ceria is an active phase that directly catalyzes methane electro-oxidation, even without the additional metal catalysts. For example, Barnett et al. found that adding a La-doped ceria layer can substantially promote direct methane oxidation in Ni-YSZ anodes.<sup>[6a]</sup> More evidence was provided by Gorte et al., who found that ceria is responsible for direct methane electro-oxidation using a Cu/ceria anode, with Cu as an electronic conductor, though it performed poorly as a methane activation catalyst, in contrast to Ni.<sup>[6b,c]</sup> Later, Knapp and Ziegler theoretically predicted that the strong interaction of CH<sub>4</sub> with the ceria (111) surface leads to the complete dissociation of CH<sub>4</sub> into CO<sub>2</sub> and H<sub>2</sub>O.<sup>[10]</sup>

In contrast, other researchers claimed that ceria has an insufficient electro-catalytic activity to provide direct methane oxidation based on the poor performance of Gd-doped ceria anodes at 1000 °C and/or the low turnover frequencies of reduced ceria for CH<sub>4</sub> conversion in the temperature range of 700–800 °C.<sup>[11]</sup> To the best of our knowledge, despite numerous research efforts, the mechanism of the direct electrochemical oxidation of CH<sub>4</sub> at the ceria/gas interface has not been clarified. Therefore, there is no effective solution to promote CH<sub>4</sub> electrochemical oxidation, which is known to be more sluggish than that associated with H<sub>2</sub>. It remains challenging to reach SOFC performance levels with CH<sub>4</sub> that are comparable to those with H<sub>2</sub> fuel.

Progress towards direct CH<sub>4</sub> fuel cells based on the fundamental insights has been hampered by several factors, including the complexity of the electrode structures and reactions, and the lack of information about the electrode surface states.<sup>[12]</sup> A typical SOFC electrode is a porous composite of a metal, primarily Ni, and an oxide electrolyte. The chemical/structural heterogeneity of the electrode makes it difficult for researchers to identify the active sites of electrode reactions or separating only surface reactions from the bulk (or gas phase) transport. Moreover, various chemical reactions can simultaneously or preferentially take place through the active metal phase, adding to the complexity of the reaction pathways. For example, highly endothermic steam reforming (CH<sub>4</sub> + H<sub>2</sub>O → 3H<sub>2</sub> + CO, ΔH<sub>25°C</sub><sup>o</sup> = 206 kJ mol<sup>-1</sup>), dry reforming (CH<sub>4</sub> + CO<sub>2</sub> → 2H<sub>2</sub> + 2CO, ΔH<sub>25°C</sub><sup>o</sup> = 247 kJ mol<sup>-1</sup>), as well as exothermic water-gas-shift reaction (CO + H<sub>2</sub>O → CO<sub>2</sub> + H<sub>2</sub>, ΔH<sub>25°C</sub><sup>o</sup> = -41.2 kJ mol<sup>-1</sup>)

can also occur with commonly used humidified methane at high temperatures. Accordingly, electrochemical oxidation of the resulting reformates, in addition to CH<sub>4</sub>, may occur primarily in the composite anodes. Significantly, observation of dynamic surface states such as adsorbates, transient intermediates, oxidation states on the ceria surface as a function of the operating conditions has been used for identifying of the active reaction sites or the rate-determining steps.<sup>[13]</sup> In fact, high-temperature electrochemistry of ceria-based electrodes in H<sub>2</sub>/H<sub>2</sub>O or CO/CO<sub>2</sub> has been explored by in operando ambient-pressure XPS (AP-XPS).<sup>[14]</sup> Although these studies have successfully elucidated the nature of the gas/ceria interfaces or the reaction pathways, it has not been yet reported for CH<sub>4</sub>/ceria electrochemical interfaces.

To address these issues, we present a model electrochemical cell which selectively monitors the direct CH<sub>4</sub> electro-oxidation reaction on Sm<sub>0.2</sub>Ce<sub>0.8</sub>O<sub>1.9-δ</sub> (SDC) thin-film electrode surfaces and which is prepared by pulsed laser deposition (PLD) and a metal lift-off process (Figure 1). Using a thin and dense mixed conducting electrode capable of sufficient current collecting and bulk ionic transport causes most of the overpotential to be applied to the SDC surface; therefore, the measured AC impedance reflects the surface reactivity. Furthermore, the metal-catalyzed chemical reactions are essentially suppressed by embedding metal current collectors within the SDC films (thickness of 600 nm), while the ceria-catalyzed reactions can be considered trivial when an anodic overpotential is applied, as detailed in the supplementary information. We also perform real-time analyses of the surface adsorbates and lattice ions during CH<sub>4</sub> electro-oxidation using synchrotron-based ambient pressure-XPS (AP-XPS). These results, in combination with density functional theory (DFT) calculations, enable us to corroborate that the SDC surface is inherently active towards C–H cleavage and that the formation of H<sub>2</sub>O limits the overall reaction rate in contrast to the previously accepted CH<sub>4</sub> activation.

## 2. Results and Discussion

### 2.1. Direct CH<sub>4</sub> Electrooxidation Pathway

CH<sub>4</sub> electrochemical oxidation on the ceria surfaces proceeds by the Mars-van Krevelen mechanism, with ceria being reduced by the fuel and then re-oxidized by oxygen ions from the electrolyte. The corresponding reaction can be written as



where O<sup>2-</sup> is an oxygen ion and Ce<sup>3+</sup> denotes a localized electron. While the actual reaction pathway involves multiple complicated steps, it can be divided into three main processes. First, the methane molecule adsorbs onto the oxide surface, and then hydrogen atoms dissociate from the molecule (Equations 2 and 3). The dissociated hydrogen binds to surface oxygen as a surface hydroxyl group or an OH<sup>-</sup> adsorbate (\*H<sub>ad</sub>, hereafter \* indicates surface O adsorption sites). Second, an adsorbed hydrogen associates with neighboring hydroxyl to form an adsorbed H<sub>2</sub>O species in which two hydrogens are combined on the surface oxygen atom. Then, the H<sub>2</sub>O molecule desorbs from the surface,

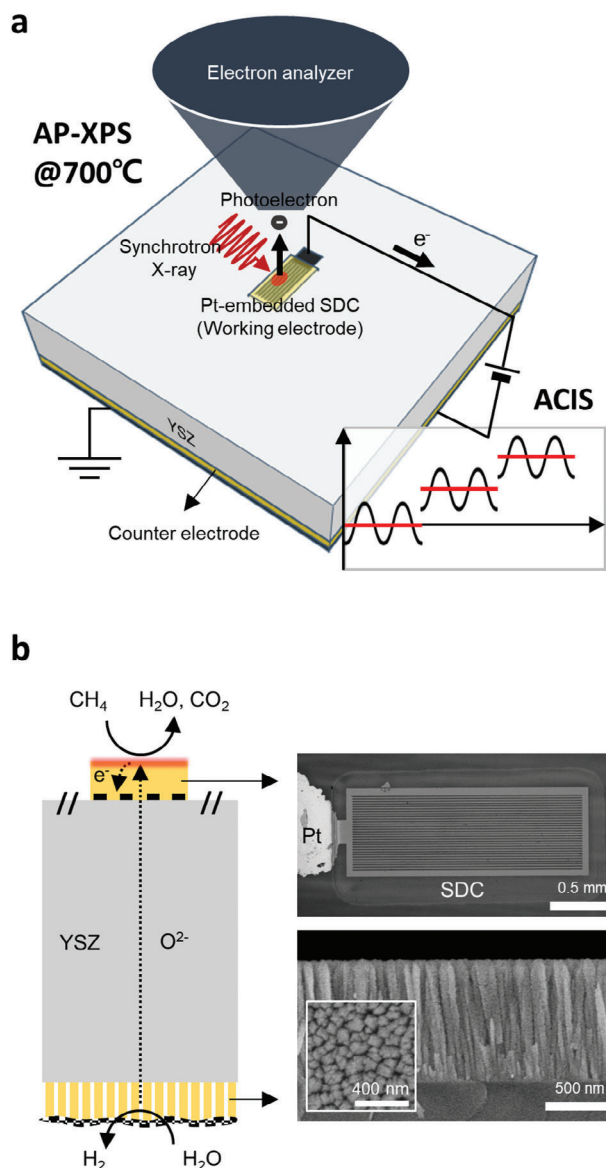
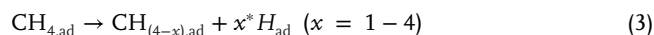


**Figure 1.** Model electrochemical cell and experimental set-up. a) Schematic illustration of model electrochemical cells composed of a single-crystal yttria-stabilized zirconia (YSZ) electrolyte, a Pt-embedded Sm-doped ceria (SDC) thin-film working electrode (WE), and a nanocolumnar SDC/Pt counter electrode (CE). b) A cross-sectional depiction of cell structures with dominant reactions at each component under an anodic overpotential ( $\eta > 0$ ), and optical and electron microscope images of WE and CE, respectively.

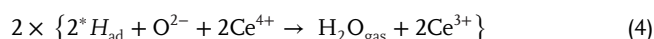
leaving an oxygen vacancy and two electrons per  $\text{H}_2\text{O}$  molecule (Equation 4). Third, the fully dissociated carbon is oxidized by the lattice oxygen to form carbon dioxide, leaving two oxygen vacancies and four electrons in the ceria lattice (Equation 5). The generated oxygen vacancies are filled with oxygen ions migrated from the electrolyte at a certain point. The electrons are delivered to the current collector, ending the overall electrode reaction (Figure 2). Here, we note that each equation does not necessarily indicate the actual presence of these intermediate species. Particularly for the formation of  $\text{CO}_2$ , more detailed routes by the CO

rebound mechanism<sup>[10]</sup> or carbonate formation<sup>[14c]</sup> can also be found in the literature.

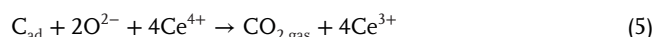
(i)  $\text{CH}_4$  adsorption and dissociation (generally known as methane activation)



(ii)  $\text{H}_2\text{O}$  formation and desorption



(iii)  $\text{CO}_2$  formation and desorption



## 2.2. AC Impedance Spectroscopy

The model electrochemical cells were characterized by AC impedance spectroscopy in  $\approx 3\%$  humidified  $\text{CH}_4$  atmospheres (9.7 to 97%  $\text{CH}_4$ ) at temperatures between 550 and 650 °C. For comparison, we repeated the measurements for wet  $\text{H}_2$ . As shown in Figure 1, the working electrode used in this study has a much smaller active area than the counter electrode, accounting for most of the electrode impedance. In addition, the narrow distance between the Pt current collecting patterns as well as the thin SDC electrode enables barrier-free electron and ion transport, respectively. Thus, the SDC electrode surface responses determine the overall cell impedance, except for the relatively small ohmic and charge transfer resistances caused by the YSZ electrolyte and the SDC/YSZ interface, respectively<sup>[15]</sup>; most of the overpotential is applied at the SDC/gas interface. Additionally, the structural stability of the electrode is crucial for precise analysis at high temperatures. We have confirmed that the structure of this model electrochemical cell is well maintained even after exposure to various atmospheres and successive polarization resistance tests (Figure S1, Supporting Information). Figure 3a shows typical impedance spectra obtained in wet  $\text{CH}_4$  at 650 °C, consisting of a large semicircle at a lower frequency along with a series consisting of offset resistance and another small semicircle at a higher frequency. As expected, only  $R_{\text{LF}}$ , displayed as the diameter of the arc at the lower frequency, is sensitive to the change in the overpotential (Figure 3a) and the gas partial pressure, as discussed in detail below. Based on these results, one can conclude that the arc at the lower frequency reflects the characteristics of the electrochemical reactions occurring at the SDC/gas interface.<sup>[9b,14b,16]</sup> Here, the overpotential values of the SDC working electrode surface were obtained as follows,

$$\eta = \Delta V - iR_{\text{ohmic}} \quad (6)$$

where  $\Delta V$  is the applied bias,  $i$  is the current throughout the electrochemical cells, and  $R_{\text{ohmic}}$  is the ohmic resistance.

Significantly, by analyzing the capacitance of the low-frequency arc,  $C_{\text{LF}}$ , we proved that the overpotential of the SDC electrode surface was accurately controlled. A large magnitude of  $C_{\text{LF}}$ , ranging from 4 to 23  $\text{mF cm}^{-2}$  in the  $\text{CH}_4\text{-H}_2\text{O}$  environment, is an indicator of a mixed conducting electrode, referred

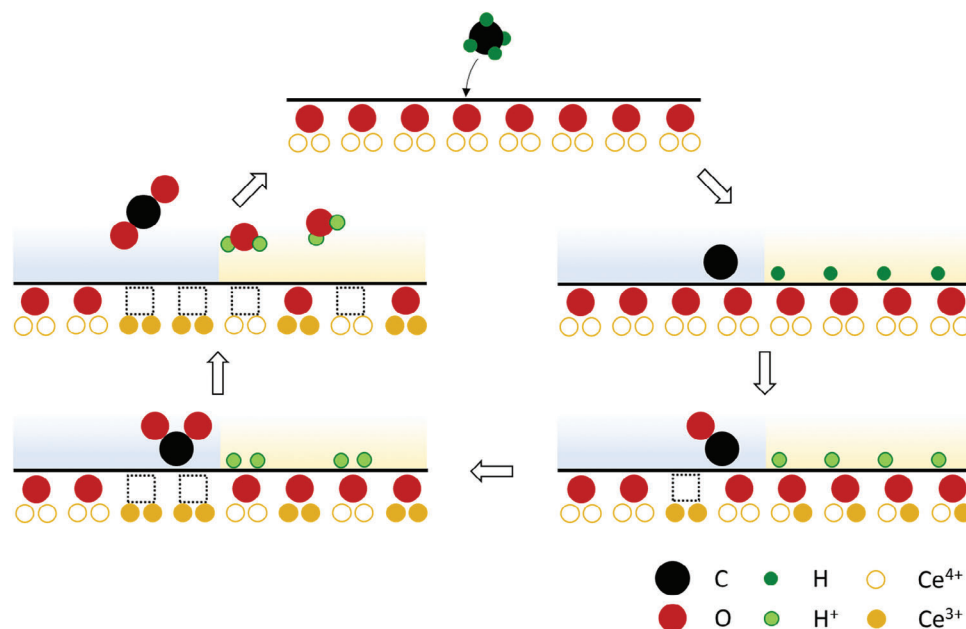


**Figure 2.** Schematic illustration of the direct  $\text{CH}_4$  electro-oxidation pathway on the mixed ionic and electronic conducting Sm-doped  $\text{CeO}_{2-\delta}$  (SDC) electrode surface. Note: since a surface-reaction-limited electrochemical cell is adopted in this study, the generated oxygen vacancies and electrons do not accumulate and are quickly filled with oxygen ions or delivered to a current collector, respectively.

to as the chemical capacitance ( $C_{\text{Chem}}$ ).<sup>[8c,17]</sup> Since the chemical capacitance depends on the oxygen chemical potential, it should change according to the equilibrium oxygen partial pressure and the applied overpotential (by the Nernst equation) if the working electrode is surface limited.<sup>[18]</sup> As shown in Figure 3b, the  $C_{\text{LF}}$  value represents the  $\text{pO}_2^{-1/4}$  dependence in a double-logarithmic plot at both the OCV and under biased conditions, regardless of the type of gas ( $\text{CH}_4$  vs  $\text{H}_2$ ). These results imply that the overpotential is primarily applied to the working electrode surface and that the variation in the anodic bias controls the oxygen chemical potential of the SDC film and the surface reaction rate on the SDC surface. On the other hand, the observed change in oxidation state due to anodic polarization may reduce the bulk electronic conductivity, potentially impacting the overall electrode processes. However, the absence of a Warburg-like diffusion response across the entire range of overpotentials suggests that electron migration is not rate-limiting. Also, its impact was previously estimated trivial by Chueh et al. in studies on similar electrode geometries.<sup>[9b,14b]</sup> As will be discussed later, in the  $\text{CH}_4$  atmosphere, under similar vapor and bias conditions, the SDC electrode is less reduced, having relatively higher levels of the effective  $\text{pO}_2$ , compared to  $\text{H}_2$ .

Next, to support the contention that  $R_{\text{LF}}$  solely represents the direct  $\text{CH}_4$  electro-oxidation processes apart from additional chemical reactions, we analyzed the compositions of the effluent gas at the open-circuit voltage, where a wet methane fuel (97% $\text{CH}_4$ -3% $\text{H}_2\text{O}$ ) was input. Only an amount of approximately 0.4%  $\text{H}_2$  was detected, whereas the  $\text{H}_2$  content predicted by the thermodynamic equilibrium for  $\text{CH}_4$  steam reforming is 9%. Such concentrations of reformed gases are too low to compete with the primary reaction with  $\text{CH}_4$ , as noted by Barnett et al.<sup>[6a]</sup> In addition, given the low catalytic activity of the bare SDC to the steam reforming reaction (Figure S2, Supporting

Information),<sup>[19]</sup> most are probably formed by the electrical wires or the counter electrodes, where they can be flushed readily from the cell by the high fuel flow rate used in this study. The high applied current density causes the observed electrode surface impedance to be dominated by electrochemical reactions, not by chemical reforming reactions. At an applied bias of +0.2 V (positive values corresponding to electro-oxidation), the current density of  $2.0 \text{ mA cm}^{-2}$  through the cell implies that the conversion of  $\text{CH}_4$  by oxygen ions is nearly 130 times more than the steam reforming of  $\text{CH}_4$  on the SDC surface (see Supporting Information). Notably, another side reaction, carbon coking, does not occur in our model electrochemical cells, as shown later by in operando surface observation.

Returning to the electrode resistance, Figure 3c is an Arrhenius plot showing how the resistance normalized to the SDC surface area ( $\bar{R}$ ) varies with temperature in both wet  $\text{H}_2$  and wet  $\text{CH}_4$  atmospheres, respectively. Despite previous studies showing that the electrode reaction rate is slower for  $\text{CH}_4$  than  $\text{H}_2$ , no attempt has been reported which quantifies exactly how the electrochemical reactivity at the ceria surface varies with the choice of gas ( $\text{H}_2$  vs  $\text{CH}_4$ ), which differentiates from side reactions and carbon coking. Therefore, Figure 3c is the first report comparing the direct electro-oxidation of  $\text{CH}_4$  with  $\text{H}_2$ . For 3% humidified  $\text{CH}_4$  at  $650^\circ\text{C}$ , an  $\bar{R}$  value of  $46.6 \pm 14.0 \Omega \text{ cm}^2$  was achieved, which is nearly 11 times greater than that obtained under 3% humidified  $\text{H}_2$ , i.e.,  $4.1 \pm 0.9 \Omega \text{ cm}^2$ . On the other hand, despite roughly the one order of magnitude difference in the surface reactivity between  $\text{CH}_4$  and  $\text{H}_2$  molecules, it can be seen that both activation energy ( $E_A$ ) values, extracted from the slopes in Figure 3c, are nearly identical. This result suggests that both reactions may share a similar rate-determining step. Considering that no carbon species are involved in  $\text{H}_2$  electro-oxidation, this observation indicates that the mutually common  $\text{H}_2\text{O}$  formation step

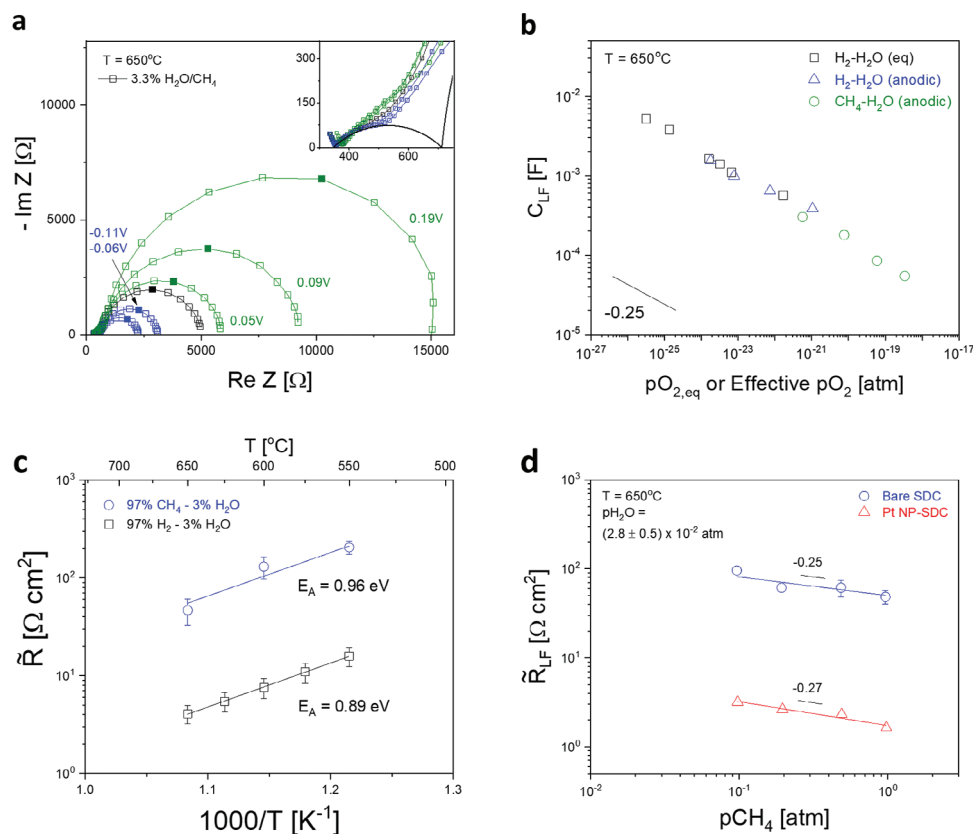


**Figure 3.** Electrochemical analysis of the SDC model electrochemical cells. a) Typical impedance ( $Z$ ) spectra measured at 650 °C, 3.3%  $\text{H}_2\text{O}$ –96.7%  $\text{CH}_4$  with different overpotentials ( $\eta$ ) ranging from  $-0.11$  to  $0.19$  V. The overpotential value was estimated by  $\eta = \Delta V - iR_{\text{ohmic}}$ . b) Double-logarithmic plot of the capacitance of a SDC working electrode versus  $p\text{O}_2$ , where the  $p\text{O}_2$  values are determined either by the gas-phase equilibrium or the overpotential. c) Arrhenius plot of  $\tilde{R}$  ( $= R_{\text{LF}}$  normalized to the SDC area) versus  $1000/T$  obtained in wet  $\text{CH}_4$  (3%  $\text{H}_2\text{O}$ –97%  $\text{CH}_4$ ) and wet  $\text{H}_2$  (3%  $\text{H}_2\text{O}$ –97%  $\text{H}_2$ ). d)  $\tilde{R}$  as a function of the methane partial pressure (with  $p\text{H}_2\text{O}$  held constant at  $(2.8 \pm 0.5) \times 10^{-2}$  atm). Metal-embedded SDC ( $\circ$ ); metal-embedded SDC with Pt nanoparticles ( $\triangle$ ). Here,  $\tilde{R}$  represents the resistance normalized to the SDC surface area.

between the two reactions is more likely to determine the overall reaction rate.

Figure 3d is a double-logarithmic plot of the resistance normalized to the SDC surface area ( $\tilde{R}_{\text{LF}}$ ) versus  $p\text{CH}_4$  with fixed  $p\text{H}_2\text{O}$  at 650 °C. The poor performance of  $\text{CH}_4$ -fueled anodes often stems from the low catalytic activity toward C–H bond activation. As such, if the elemental steps associated with molecular  $\text{CH}_4$ , such as adsorption or dissociation, are the rate-limiting steps (Equations 2 and 3), the empirical reaction order in the rate equation,  $v = p\text{CH}_4^n$ , is generally expected to be proportional to  $p\text{CH}_4$  with a power-law exponent ( $n$ ) of about  $-1$ .<sup>[20]</sup> However, the observed power-law dependence corresponding to the slope value is relatively small at approximately  $-0.25$ , suggesting that the rate-determining step (RDS) is largely independent of the  $\text{CH}_4$  activation step. To confirm this, we examined how the electrode impedance changes when Pt nanoparticles are added to the SDC surface. Because Pt is an excellent catalyst for  $\text{CH}_4$  adsorption/dissociation,<sup>[21]</sup> the introduction of Pt was expected to significantly reduce both the electrode resistance and the reaction order with respect to the  $\text{CH}_4$  partial pressure. However, as shown in Figure 3d, the  $p\text{CH}_4$  dependence remained constant while the observed electrode resistance was greatly reduced by a factor of 1/21. These observations suggest that although Pt sig-

nificantly enhances  $\text{CH}_4$  electro-oxidation, its primary role is not to promote the elementary steps of  $\text{CH}_4$  activation.

### 2.3. Ambient-Pressure XPS

For more substantial support of this hypothesis and to identify the RDS of the  $\text{CH}_4$  electrochemical oxidation process, the compositions and variations of the intermediate species present on the SDC electrode surface were monitored using ambient-pressure XPS. The photoemission spectra were collected from the SDC surface with the overpotential between  $-0.09$  to  $+0.33$  V applied to the SDC working electrodes in a mixture of 210 mTorr  $\text{CH}_4$  and 10 mTorr  $\text{H}_2\text{O}$  gases at 700 °C. To avoid hysteresis, the measurement was performed after achieving a steady state, as confirmed by current stabilization at each potential (Figure S3, Supporting Information).

Figure 4a,b correspondingly show the C 1s and O 1s photoemission spectra at the probing depth of  $\approx 0.6$  nm. In the C 1s spectra (Figure 4a), the relatively broad peak at 290 eV is determined to be the Ce 4s core-level peak,<sup>[22]</sup> as evidenced by the spectra for the clean SDC surface exposed to 150 mTorr  $\text{O}_2$ . The sharp primary peak at  $\approx 286$  eV is attributed to gas-phase  $\text{CH}_4$ ,

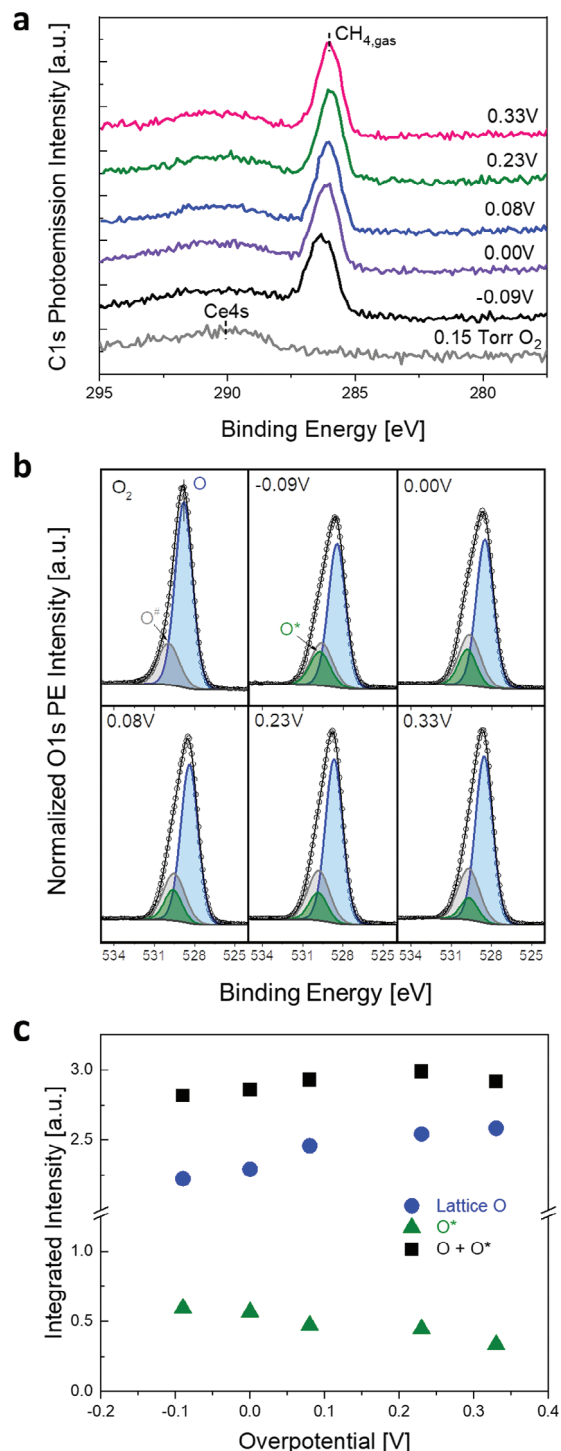


**Figure 4.** Responses of the intermediate species to the overpotential (−0.09 to 0.33 V) in 200 mTorr CH<sub>4</sub> and 20 mTorr H<sub>2</sub>O at ≈700 °C. a) C 1s photoemission spectra obtained at a photon energy of 490 eV. b) Normalized O 1s photoemission spectra obtained at a photon energy of 690 eV. The kinetic energies of the C 1s and O 1s photoelectrons were controlled to have a probing depth of ≈0.6 nm. The three peaks correspondingly indicate lattice oxygen (blue O), Si impurities (gray O<sup>#</sup>), and intermediate \*H<sub>ad</sub> species (O\*). c) The normalized peak areas of O and O\* as a function of the overpotential.

consistent with the peak assignment in the literature.<sup>[22b,c]</sup> The first notable feature from the data is that peaks corresponding to carbon-related adsorbates or intermediates such as CH<sub>x</sub> (285 eV<sup>[22b,c]</sup>), carbonates (CO<sub>3</sub><sup>2−</sup>, ≈290 eV<sup>[14c,d,23]</sup>), or carboxylate (CO<sub>2</sub><sup>δ−</sup>, 286–288.5 eV<sup>[14d,24]</sup>) were not observed under the measured conditions. In contrast, several carbon-related peaks were clearly observed when a cathodic overpotential of −0.26 V was applied (Figure S4, Supporting Information). Because the presence of the reaction intermediates provides evidence that their consumption process is rate-limiting, these observations suggest that neither CH<sub>4</sub> activation nor the CO<sub>2</sub> formation are the RDS for electrochemical CH<sub>4</sub> oxidation. Second, the absence of the peak associated with graphitic carbons (approximately at ≈285 eV<sup>[25]</sup>) during all stages of the anodic overpotential indicates that carbon deposition does not occur at all on the SDC surface during CH<sub>4</sub> electro-oxidation.

On the other hand, interesting aspects were observed in the O 1s spectra (Figure 4b), which consist of a total of three peaks. The prominent peak at ≈530 eV (blue, denoted as O) is attributed to the lattice oxygen of SDC.<sup>[14a,b]</sup> The peak at a higher binding energy level by ≈1.2 eV (gray, denoted as O<sup>#</sup>) originates from Si impurities (see details in Figures S5 and S6, Supporting Information).<sup>[14b]</sup> Finally, the minor shoulder peak at a binding energy of about 1.1–1.5 eV higher than the peak O level is always present with wet CH<sub>4</sub> (green, O\*); this is attributed to an adsorbed hydroxyl group on the SDC electrodes (\*H<sub>ad</sub>).<sup>[14a]</sup> The absence of carbon species and the presence of \*H<sub>ad</sub> clearly corroborate that an elemental step during the H<sub>2</sub>O formation and desorption process determines the overall reaction rate (as shown in Equation 4). This conclusion is in good agreement with the impedance analysis mentioned earlier. Moreover, we quantify how the concentration of the oxygen species varies with the overpotential by fitting the O 1s spectra with three components (see details in the Supporting Information).<sup>[14b,26]</sup> Figure 4c summarizes the intensity of the lattice O (O) and the \*H<sub>ad</sub> intermediate (O\*) as a function of the overpotential. It is important to note that the lattice O and \*H<sub>ad</sub> species show a counter-correlation with each other in terms of their intensity change versus overpotential. As the anodic overpotential increases, the intensity of the O\* peak decreases while that of the O peak increases, and their sum is almost constant. In fact, this observation is exactly the same as the SDC electrode surface response in the H<sub>2</sub>/H<sub>2</sub>O atmosphere reported by Feng et al.,<sup>[14b]</sup> suggesting that the interaction between H<sub>2</sub>O and the surface oxygen vacancies is so facile that the H<sub>2</sub>O removal process can take place quickly when the oxygen ions migrate from the bulk to the surface (vice-versa H<sub>2</sub>O incorporation process as well). Therefore, we can further exclude the H<sub>2</sub>O desorption from the rate-determining steps, leading us to speculate that the H<sub>2</sub>O formation limits the overall reaction rate of CH<sub>4</sub> electro-oxidation.

Our findings provide clear evidence that the difference in the surface activity of SDC between H<sub>2</sub> and CH<sub>4</sub> can be due to the different rate of H<sub>2</sub>O formation rather than the elementary steps involving two different molecules, e.g., adsorption or dissociation. Chemically, the H<sub>2</sub>O formation rate should be linked to the concentration of \*H<sub>ad</sub> that subsequently combine to form H<sub>2</sub>O molecules. Moreover, since \*H<sub>ad</sub> is an active site for the rate-limiting H<sub>2</sub>O formation during the electrode processes,

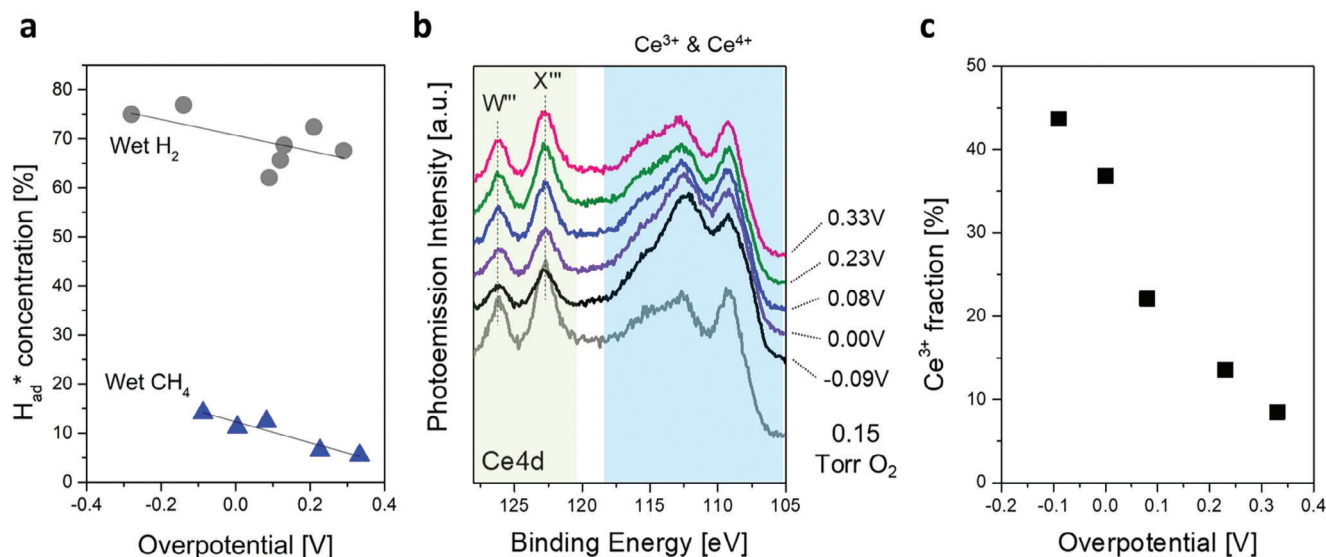


**Figure 5.** a) Concentration of  $H_{ad}^*$  species in humidified  $H_2$  and  $CH_4$  environments. The concentration was estimated by an areal fitting of the lattice O (O) and hydroxyl group (O\*) in O 1s photoelectron spectra obtained in the similarly humidified atmospheres. b) Ce 4d photoemission spectra as a function of overpotential obtained at a photon energy of 370 eV in 200 mTorr  $CH_4$  and 20 mTorr  $H_2O$  at  $\approx 700$  °C. The kinetic energy was controlled to have a probing depth of  $\approx 0.6$  nm. c)  $Ce^{3+}$  concentration determined from Ce 4d spectra.

variations in their concentrations can be indicative of catalytic activities. Thus, we compared the  $H_{ad}^*$  concentration on SDC under a similarly humidified  $H_2$  and  $CH_4$  atmosphere (Figure S7, Supporting Information). Figure 5 summarizes the results of the relative  $H_{ad}^*$  concentration, defined as  $100 \times [O^*] / ([O] + [O^*])$ , as a function of overpotential. It confirms that a much higher  $H_{ad}^*$  concentration is present on the SDC surface in  $H_2$  than  $CH_4$ . For instance, the concentration of  $H_{ad}^*$  is 67.7% at 0.29 V in  $H_2$  while it is 5.5% at 0.33 V in  $CH_4$ . In fact, with the similarity of the reaction pathways for  $H_2$  and  $CH_4$  fuels we revealed, this may not be surprising considering that the amount of  $H_{ad}^*$  is correlated to that of surface oxygen vacancies that are quasi-equilibrated with the bulk.<sup>[26]</sup> That is, by either chemically ( $pO_{2,eq}$ ) and/or electrochemically ( $pO_{2,eff}$ ), the  $H_2$  atmosphere provides a more reduced state of SDC such that the accumulation of oxygen vacancies in the surface region is more pronounced.

In addition to  $H_{ad}^*$  species,  $Ce^{3+}$  is another important intermediate as a mobile charge (small polaron) that is coupled with electrogenerated oxygen vacancies in the electrochemical reaction (Equations 4 and 5). Figure 5b shows the Ce 4d photoemission spectra with 3+ and 4+ multiplet splitting, obtained at the same 0.6 nm information depth as O1s and C1s, and Figure 5c presents the calculated concentration of  $Ce^{3+}$  (see details in Figure S8, Supporting Information), plotted against overpotential. This clarifies that the anodic overpotential effectively oxidizes the electrode surface, and this change is significant. Unlike the minimal impact of the decrease in  $Ce^{3+}$  on electronic conductivity observed in impedance, these changes could be a major factor determining the surface reactivity (Figure 3a). For example, these species are negatively charged, and the electrical double layer formed between  $Ce^{3+}$  and positively charged surface adsorbates ( $H_{ad}^*$ ) can play an important role in electrochemical reactions.<sup>[14d,27]</sup> Particularly, their overpotential-dependent surface dipole potential can modulate the charge transfer rates.<sup>[27]</sup>

Also notable is that the concentration of surface  $Ce^{3+}$  is still substantially high even under such high oxidizing current (8.5% at 0.33 V). W. Chueh et al. also observed similar trends in SDC under  $H_2$ - $H_2O$  environments, and suggested that reduced SDC surfaces with relatively abundant  $Ce^{3+}$  in nearly oxygen-vacancy-free conditions under anodic overpotential may play a crucial role in the electro-oxidation of  $H_2$ .<sup>[14b]</sup> Often, such reduced SDC surfaces are considered the origin of the unique electro-catalysis of ceria-based materials.<sup>[17,28]</sup> These results are consistent with our findings that electron transfer from Pt to SDC through the interaction with Pt nanoparticles significantly enhances the activity around the rim area and greatly increases the rate of  $H_2O$  formation.<sup>[16b]</sup> Similarly, the atomic local structures around  $Ce^{3+}$  in Pt-decorated ceria catalysts have been identified as the basis for their superior catalytic performance.<sup>[29]</sup>

## 2.4. Theoretical Investigation

The energetics of  $CH_4$  dissociative adsorption estimated on both the bare ceria and SDC surfaces show that  $CH_4$  activation is relatively facile on SDC (Figure 6a). The activation energy barrier,  $E_A$ , of 0.97 eV calculated on bare ceria predicts that  $CH_4$  activation is sluggish and likely sensitive to the partial pressure of  $CH_4$  in the reaction feedstock. On the other hand, the barrierless spontaneous adsorption of  $CH_4$  is available on SDC with an 80% increased  $H_{ad}$  than ceria ( $E_{ad} = -3.90$  eV), suggesting that SDC potentially catalyzes  $CH_4$  dissociation and the subsequent oxidation (Figure 6a).

We estimated the sequential pathway of  $CH_4$  dissociation and  $CO_2$  production with a dissociatively adsorbed  $CH_4$  molecule in the vicinity of the Sm dopant (Figure 6b). All hydrogen abstraction from  $CH_4$  are exothermic with corresponding  $E_A$  values. Although the final  $CO_2$  desorption is endothermic ( $\Delta E_5 = 0.58$  eV),

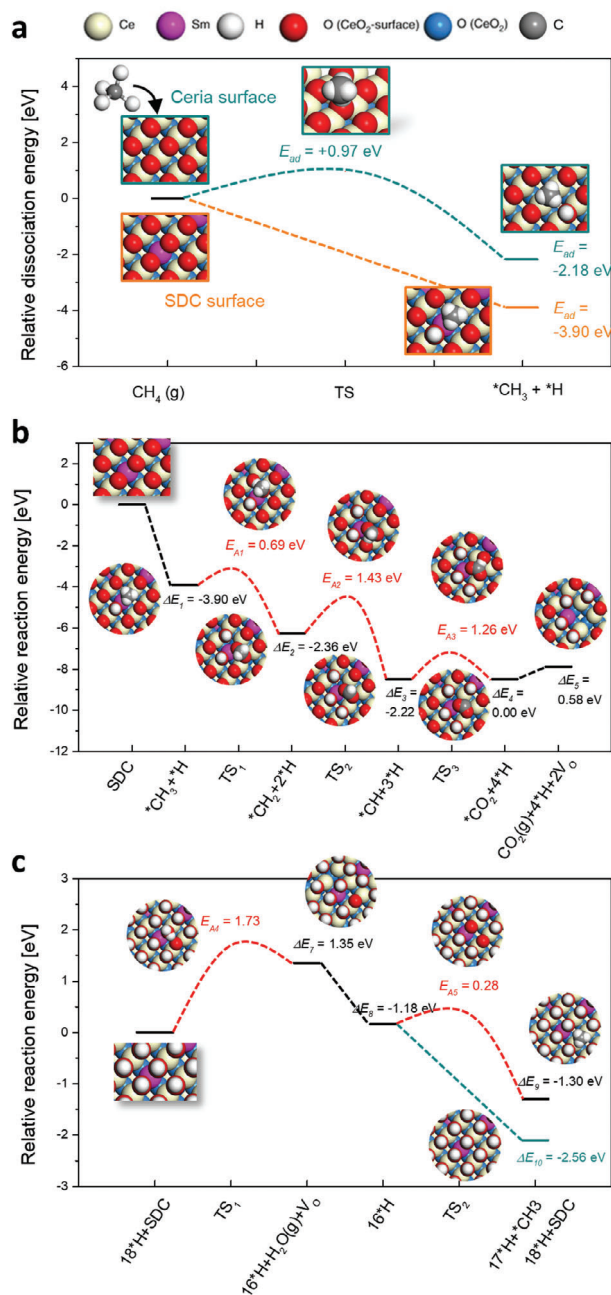


**Figure 6.** DFT-estimated energetics of CH<sub>4</sub> oxidation. a) Dissociative adsorption of CH<sub>4</sub> on ceria and SDC. b) Full reaction pathway of CH<sub>4</sub> dissociation and CO<sub>2</sub> production (c) H<sub>2</sub>O formation on the H-saturated SDC surface. The blue dotted line and the corresponding ΔE<sub>10</sub> present the case of H<sub>2</sub> binding after H<sub>2</sub>O production. The E<sub>A</sub> and ΔE<sub>n</sub> denote the activation energy barrier and reaction energy of the n<sup>th</sup> step, respectively. The adsorbed species on the surface are denoted with asterisks (\*).

the entropic contribution to the free energy of CO<sub>2</sub> desorption overcomes this enthalpy increase.<sup>[30]</sup> The calculated E<sub>A</sub> values of CH<sub>4</sub> dissociation with the maximum of 1.43 eV (E<sub>A2</sub>) suggest that the dissociation becomes facile as a function of the reaction temperature and the CH<sub>4</sub> partial pressure. However, because the DFT-calculated E<sub>A</sub> is sensitive to the local atomic ensemble of

the reaction sites,<sup>[31]</sup> the calculated E<sub>A</sub> values could decrease as the abstracted protons diffuse along the SDC surface (Figure S9, Supporting Information). Upon the final CO<sub>2</sub> release from SDC, note that two oxygen vacancies, V<sub>o</sub>, are formed (the final stage, Figure 6b). These vacancies can be healed by the transferred oxygen ions from the electrodes.

Because each CH<sub>4</sub> molecule produces four hydroxyls on SDC, we further constructed the fully covered SDC surface with protons and estimated the energetics of H<sub>2</sub>O production (Figure 6c). The H<sub>2</sub>O formation and production were endergonic (ΔE<sub>7</sub> = 1.35 eV) with E<sub>A</sub> of 1.73 eV, showing that H<sub>2</sub>O formation is indeed the RDS of CH<sub>4</sub> oxidation. Even though the entropic acceleration of H<sub>2</sub>O desorption also occurs like the case of CO<sub>2</sub> desorption, such high E<sub>A</sub> means that H<sub>2</sub>O formation is slow. As a result, the abstracted protons from CH<sub>4</sub> molecules may occupy a significant fraction of the SDC surface under the reaction condition and are responsible for the \*H<sub>ad</sub>-related peaks in the AP-XPS spectra. The calculated E<sub>ad</sub> of binding of CH<sub>4</sub> (ΔE<sub>9</sub> = -1.30 eV) and H<sub>2</sub> (ΔE<sub>10</sub> = -2.56 eV) on the open space formed after H<sub>2</sub>O desorption shows that H<sub>2</sub> becomes the main adsorption species (Figure 6c). This result supports our experimental finding that the  $\tilde{R}$  of H<sub>2</sub> oxidation is lower than CH<sub>4</sub> oxidation despite the similar E<sub>A</sub> in both cases (Figure 3c) and that the concentration of the \*H<sub>ad</sub> is greater under the H<sub>2</sub> fuel stream (Figure 5). Our DFT-estimated reaction pathway of CH<sub>4</sub> dissociation, CO<sub>2</sub> production, and H<sub>2</sub>O formation on SDC reproduces the experimental findings discussed above that CO<sub>2</sub> production is relatively facile, and H<sub>2</sub>O production is the RDS of CH<sub>4</sub> oxidation. Although the oxygen vacancies formed in the reaction pathway are quickly filled by overpotential as we have observed, it can be assumed an inherent or dynamically defective surface where oxygen vacancies may still exist. We confirmed whether the overall reaction pathways on this O-vacated SDC surface still yield the similar results. The CH<sub>4</sub> dissociation on the O-vacated SDC surface still occurs spontaneously around the Sm sites with slight energy differences (Figure S10a, Supporting Information), and the formation of H<sub>2</sub>O remains the rate-determining step (Figure S10b, Supporting Information). Therefore, both the dynamically changing SDC surface and the surface simulated based on our APXPS observations support our hypothesis regarding the reaction pathway.

Choi et al. showed that the step-by-step response of the electronic structure under the H<sub>2</sub> oxidation condition of the SDC combined with noble metal nanoparticles provides an insight into the local electronic state of the reaction sites.<sup>[16b]</sup> The electronic structure analysis results in Figure S11b (Supporting Information) show that the adjacent lattice oxygen ion of SDC to the Sm dopant is electron-depleted, becoming highly hydrogenphilic, confirming our DFT calculation results. Once all lattice oxygen ions of SDC are saturated with protons, the electrons donated from hydrogen reduce the Ce and lattice oxygen ions (Figure S11c, Supporting Information), indicating the formation of Ce<sup>3+</sup>. This result shows that the concentration of surface Ce<sup>3+</sup> is correlated with the concentration of \*H<sub>ad</sub>, potential-driven surface oxygen vacancies saturated with hydroxyl species, during the reactions, which is in good agreement with the APXPS observations in Figure 5. Moreover, this finding highlights our experimental result that the extent of electronic reduction of SDC is vital in determining the performance of ceria-based anode.

Interestingly, the local electronic structure of the SDC after H<sub>2</sub>O desorption and vacancy healing reproduces the electronic ensemble of pristine ceria even in the presence of the Sm dopants (Figure S11d, Supporting Information). This finding suggests that H<sub>2</sub>O formation is a phenomenologically appropriate rate-limiting step on SDC under both H<sub>2</sub>- and CH<sub>4</sub>-fueled conditions.

### 3. Conclusion

In summary, we investigated the direct CH<sub>4</sub> electro-oxidation reaction at the gas/ceria electrochemical interfaces by combined experiments and DFT calculations. We clearly differentiated the experimental responses from the miscues due to the microstructural and reaction complexities associated with the conventional anodes with thin-film model electrochemical cells. Our results revealed that the H<sub>2</sub>O formation step limits the overall reaction rate in CH<sub>4</sub> electro-oxidation process rather than C–H cleavage or CO<sub>2</sub> formation. Under similar reaction pathways sharing the RDS in H<sub>2</sub> and CH<sub>4</sub> fuels, a direct comparison of surface OH concentration clarified that how much SDC surface can be reduced is one major factor determining the performance of ceria-based anode. Our conclusion thus far suggests potential strategies to enhance the surface activity of SDC electrodes when directly utilizing CH<sub>4</sub> as a fuel in SOFCs. Contrary to the conventional idea that facilitating the adsorption or dissociation of CH<sub>4</sub> molecules can promote the electrode reaction rate, our results put more emphasis on the degree of reduction of the SDC surface. For example, co-feeding a small amount of H<sub>2</sub> into CH<sub>4</sub> might be beneficial in reducing the ceria surface. Decorating metal nanoparticles that electronically interact with ceria electrodes can also be one way to reduce ceria surface. This study provides an unambiguous clue to the direct electro-oxidation of CH<sub>4</sub> and answers a longstanding debate on the electrocatalysis of ceria for CH<sub>4</sub> oxidation.

### 4. Experimental Section

**Sample Preparation:** 1 μm thick Sm<sub>0.2</sub>Ce<sub>0.8</sub>O<sub>1.9</sub> (SDC) nanocolumnar thin-film was fabricated by PLD (KrF 248 nm excimer laser, Lambda Physik 205, 270 mJ, 20 Hz) onto one-side of (100) single-crystal YSZ substrate (10 × 10 × 0.5 mm<sup>3</sup>, MTI Corp.) to serve as the counter electrode. The deposition temperature was 600 °C and working pressure of the chamber filled with oxygen gas (99.999%) was 100 mTorr. Then, 100 nm-thick Pt thin-film was deposited by DC magnetron sputtering (a DC power of 100 W, a working pressure of 10 mTorr Ar) for current collection.<sup>[32]</sup> Next, the working electrode was fabricated on the other side of the YSZ substrate. A 120 nm thick Pt patterned current collectors were first obtained through a photolithographic lift-off process. A positive photoresist (AZ5214) was spin-coated onto SDC films at 3000 rpm and baked at 115 °C for 1 min. The samples were exposed to UV light for 6 s in contact with a photomask having defined metal patterns after being aligned by a contact aligner (MDA-8000B, MIDAS Corp.). Then, the samples were immersed in a developer (AZ 300 MIF, AZ Electronic Materials Corp.) for 40 s followed by DI water rinsing, drying, and baking at 120 °C for 2 min. After Pt sputtering, the samples were immersed in acetone with mild ultrasonication to achieve final patterns. Before the deposition of dense SDC thin films, the sample was annealed at 800 °C for 2 h (5 °C min<sup>-1</sup> of heating rate) to sinter the patterns. Finally, a 600 nm thick, dense SDC film was grown onto patterned Pt/YSZ with a shadow mask with an opening of 0.9 × 2 mm<sup>2</sup>. The PLD was performed at 700 °C under 10 mTorr O<sub>2</sub> (270 mJ, 10 Hz).

**AC Impedance Spectroscopy:** The electrochemical reactions were investigated by electrochemical impedance spectroscopy (VSP-300, Biologic) under wet methane atmosphere in the temperature range of 550–650 °C. The entire cell was placed inside an alumina tube in a uniform gas atmosphere. The mixture gases (3% H<sub>2</sub>O-CH<sub>4</sub>) with a total flow rate of 50 sccm (a gas velocity of 9.85 cm min<sup>-1</sup>) controlled by digital mass flow controllers flowed into the tube. To measure the sensitivity of the impedance to the partial pressure of methane (pCH<sub>4</sub>), the ratio between CH<sub>4</sub> and N<sub>2</sub> was controlled at the fixed partial pressure of water (pH<sub>2</sub>O). The humidity of the gases was controlled by passing them through a DI water bubbler immersed in an isothermal bath, fixed at 10 °C and monitored using a humidity sensor (Rotronic Hygroflex). Here, the partial pressure of oxygen was directly measured by a home-made zirconia pO<sub>2</sub>-sensor. For electrical contact, a home-made sample stage made by alumina tube and Pt wires and Au meshes was used. The alumina tube-shielded thermocouple was placed near the sample to measure the sample temperature. The AC perturbation amplitude of ± 10 mV at anodic bias of 0, 50, 100, 200, 300 mV was used with a measurement frequency range of 0.01 Hz– 1 MHz. To avoid any cumulative effect of applied bias, the zero bias measurement was inserted before each polarization step (0 → 50 → 0 → 100 → 0 → 200 → 0 → 300 → 0 mV). For each polarization, the impedance was obtained at least after 1.5 h of the stabilization.

**In Operando X-Ray Photoelectron Spectroscopy:** The beamline 9.3.2 at Advanced Light Source (ALS), Lawrence Berkeley National Laboratory (LBNL) offers the synchrotron X-ray-based, operando XPS. A tailor-made holder was used to provide both heating and electrical contacts to the electrochemical cells.<sup>[14b]</sup> The Pt foil was placed onto the ceramic heater to electrically contact to the counter electrode. On the other hand, Pt wires were used to contact the working electrode. Soft X-ray is irradiated to the working electrode at an incident angle of 75° to the sample normal while the electron analyzer (cone) is positioned perpendicular to the sample. The counter electrode was Fermi coupled (grounded) with the electron analyzer. A piece of Au foil on top sample surface was electrically connected to the working electrode. An incident photon energy was calibrated by collecting Au 4f<sub>7/2</sub> peak (84.0 eV) before the measurements. In case, one of the multiplet splitting component of Ce<sup>4+</sup> (Ce 4d X'' peak) at the binding energy of 122.8 eV was used as the internal reference peak. The sample was heated to the target temperature of ≈700 °C in UHV. Here, the temperature was calibrated by using the externally measured YSZ electrolyte resistance. Then, 150 mTorr O<sub>2</sub> was introduced to remove the adventitious carbon on the electrode surface. After the chamber was pumped back out to UHV (≈10<sup>-8</sup> Torr), the mixture of 220 mTorr CH<sub>4</sub>/H<sub>2</sub>O (24:1), similar to that employed in a typical solid oxide fuel cells, was established. Multiple steps of the bias were applied between top working electrodes and bottom counter electrodes using a potentiostat (SP-300, Biologic) with a perturbation voltage of 20 mV. During each polarization step, the photoelectron data were collected after the stabilization to eliminate hysteretic effects, which was confirmed by impedance evolution over exposure time. The kinetic energies of photoelectrons from different elements were controlled to have similar information depth of ≈0.6 nm. The software CasaXPS was used for the fitting process. All peaks were fitted with a symmetric Gaussian-Lorentzian shape (GL(30)).

**DFT Calculations:** All generalized gradient approximation-level spin-polarized DFT calculations were carried out with the Vienna Ab initio Simulation Package (VASP) code<sup>[33]</sup> using the PBE<sup>[34]</sup> functional. The valence electron wave functions were expanded in a plane-wave basis up to cut-off energy of 400 eV. The interaction between ionic core electrons and valence electrons was described by the projector augmented-wave (PAW) method.<sup>[35]</sup> The DFT+U formalism<sup>[36]</sup> with U<sub>eff</sub> = 5 eV<sup>[16b,37]</sup> was used for Ce ions to treat the localized Ce-4f orbitals. The Brillouin zone was sampled at the Γ-point. The convergence criteria for the electronic structure and atomic geometry were set to 10<sup>-4</sup> eV and 0.03 eV Å<sup>-1</sup>, respectively. A Gaussian smearing function with a finite temperature width of 0.05 eV was used. The geometry and the energetic location of the transition state were estimated using the climbing-image nudged elastic band (CI-NEB) method.<sup>[38]</sup> The geometry of bare ceria and SDC is reported elsewhere.<sup>[16b]</sup>

## Supporting Information

Supporting Information is available from the Wiley Online Library or from the author.

## Acknowledgements

Y.C. and H.H. contributed equally to this work. Y.C. acknowledges the financial support by the Research and Development Program of the Korea Institute of Energy Research (Grant Number C4-2467) and the National Research Foundation of Korea (NRF) funded by the Ministry of Science, ICT (NRF-2021M3I3A1084931). H.Y.K. acknowledges the financial support by the National Research Foundation of Korea (NRF) grant funded by the Korean government (Ministry of Science and ICT, MSIT) (2023R1A2C2008117), the Basic Science Research Program through the NRF funded by the Ministry of Education (2021R1A6A1A03043682). W.J. acknowledges the financial support by the National Research Foundation of Korea (NRF) funded by the Ministry of Science and ICT (NRF-2023R1A2C3005190) and Ceramic Strategic Technology R&D program through the Korea Institute of Ceramic Engineering & Technology (KICET) (grant NTIS no. 1415187241).

## Conflict of Interest

The authors declare no conflict of interest.

## Data Availability Statement

The data that support the findings of this study are available from the corresponding author upon reasonable request.

## Keywords

carbon-neutral hydrocarbons, CH<sub>4</sub> (methane) electrooxidation, Sm-doped ceria (SDC), solid oxide fuel cells (SOFCs)

Received: March 11, 2024  
Revised: July 24, 2024  
Published online: August 17, 2024

- [1] A. Kirubakaran, S. Jain, R. K. Nema, *Renewable Sustainable Energy Rev.* **2009**, *13*, 2430.
- [2] U.S. Department of Energy, *Fuel Cell Handbook*, EG&G Technical Services, Inc, New York **2004**.
- [3] A. M. Abdalla, S. Hossain, O. B. Nisfindy, A. T. Azad, M. Dawood, A. K. Azad, *Energy Convers. Manage.* **2018**, *165*, 602.
- [4] a) S. McIntosh, R. J. Gorte, *Chem. Rev.* **2004**, *104*, 4845; b) W. Wang, C. Su, Y. Wu, R. Ran, Z. Shao, *Chem. Rev.* **2013**, *113*, 8104.
- [5] B. C. H. Steele, P. H. Middleton, R. A. Rudkin, *Solid State Ionics.* **1990**, *40-41*, 388.
- [6] a) E. P. Murray, T. Tsai, S. A. Barnett, *Nature.* **1999**, *400*, 649; b) R. J. Gorte, S. Park, J. M. Vohs, C. H. Wang, *Adv. Mater.* **2000**, *12*, 1465; c) S. D. Park, J. M. Vohs, R. J. Gorte, *Nature.* **2000**, *404*, 265; d) W. Zhu, C. R. Xia, J. Fan, R. R. Peng, G. Y. Meng, *J. Power Sources.* **2006**, *160*, 897; e) H. Kan, H. Lee, *Catal. Commun.* **2010**, *12*, 36; f) V. Papaefthimiou, M. Shishkin, D. K. Niakolas, M. Athanasiou, Y. T. Law, R. Arrigo, D. Teschner, M. Havecker, A. Knop-Gericke, R. Schlogl, T. Ziegler, S. G. Neophytides, S. Zafeiratos, *Adv. Energy Mater.* **2013**, *3*, 762; g) Z. M. Wang, Y. D. Li, J. W. Schwank, *J. Power Sources.* **2014**, *248*, 239.
- [7] a) X. M. Ge, S. H. Chan, Q. L. Liu, Q. Sun, *Adv. Energy Mater.* **2012**, *2*, 1156; b) X. L. Zhou, J. M. Zhen, L. M. Liu, X. K. Li, N. Q. Zhang, K. N. Sun, *J. Power Sources.* **2012**, *201*, 128; c) H. P. Ding, Z. T. Tao, S. Liu, Y. T. Yang, *J. Power Sources.* **2016**, *327*, 573.
- [8] a) H. L. Tuller, A. S. Nowick, *J. Phys. Chem. Solids.* **1977**, *38*, 859; b) V. V. Kharton, F. M. B. Marques, A. Atkinson, *Solid State Ionics.* **2004**, *174*, 135; c) W. Lai, S. M. Haile, *J. Am. Ceram. Soc.* **2005**, *88*, 2979.
- [9] a) T. Nakamura, K. Yashiro, A. Kaimai, T. Otake, K. Sato, T. Kawada, J. Mizusaki, *J. Electrochem. Soc.* **2008**, *155*, B1244; b) W. C. Chueh, Y. Hao, W. Jung, S. M. Haile, *Nat. Mater.* **2012**, *11*, 155.
- [10] D. Knapp, T. Ziegler, *J. Phys. Chem. C.* **2008**, *112*, 17311.
- [11] a) O. A. Marina, M. Mogensen, *Appl. Catal., A.* **1999**, *189*, 117; b) M. Mogensen, K. Kammer, *Annu. Rev. Mater. Res.* **2003**, *33*, 321.
- [12] L. Fan, C. e. Li, P. V. Aravind, W. Cai, M. Han, N. Brandon, *J. Power Sources.* **2022**, *538*, 231573.
- [13] X. Garcia, L. Soler, N. J. Divins, X. Vendrell, I. Serrano, I. Lucentini, J. Prat, E. Solano, M. Tallarida, C. Escudero, J. Llorca, *Catalysts.* **2020**, *10*, 286.
- [14] a) C. J. Zhang, Y. Yu, M. E. Grass, C. Dejoie, W. C. Ding, K. Gaskell, N. Jabeen, Y. P. Hong, A. Shayorskiy, H. Bluhm, W. X. Li, G. S. Jackson, Z. Hussain, Z. Liu, B. W. Eichhorn, *J. Am. Chem. Soc.* **2013**, *135*, 11572; b) Z. A. Feng, F. El Gabaly, X. Ye, Z.-X. Shen, W. C. Chueh, *Nat. Commun.* **2014**, *5*, 4374; c) Y. Yu, B. H. Mao, A. Geller, R. Chang, K. Gaskell, Z. Liu, B. W. Eichhorn, *Phys. Chem. Chem. Phys.* **2014**, *16*, 11633; d) Z. L. A. Feng, M. L. Machala, W. C. Chueh, *Phys. Chem. Chem. Phys.* **2015**, *17*, 12273; e) T. L. Skafte, Z. X. Guan, M. L. Machala, C. B. Gopal, M. Monti, L. Martinez, E. Stamate, S. Sanna, J. A. G. Torres, E. J. Crumlin, M. Garcia-Melchor, M. Bajdich, W. C. Chueh, C. Graves, *Nat. Energy.* **2019**, *4*, 846; f) L. Wang, Y. Yu, K. J. Gaskell, E. J. Crumlin, Z. Liu, B. W. Eichhorn, G. S. Jackson, *J. Phys.: Energy.* **2021**, *3*, 014004.
- [15] a) W. Jung, J. O. Dereux, W. C. Chueh, Y. Hao, S. M. Haile, *Energy Environ. Sci.* **2012**, *5*, 8682; b) T. S. Oh, S. M. Haile, *Phys. Chem. Chem. Phys.* **2015**, *17*, 13501; c) Y. Choi, E. C. Brown, S. M. Haile, W. Jung, *Nano Energy.* **2016**, *23*, 161.
- [16] a) C. Chen, D. Chen, W. C. Chueh, F. Ciucci, *Phys. Chem. Chem. Phys.* **2014**, *16*, 11573; b) Y. Choi, S. K. Cha, H. Ha, S. Lee, H. K. Seo, J. Y. Lee, H. Y. Kim, S. O. Kim, W. Jung, *Nat. Nanotechnol.* **2019**, *14*, 245.
- [17] W. C. Chueh, S. M. Haile, *Phys. Chem. Chem. Phys.* **2009**, *11*, 8144.
- [18] T. Kawada, J. Suzuki, M. Sase, A. Kaimai, K. Yashiro, Y. Nigara, J. Mizusaki, K. Kawamura, H. Yugami, *J. Electrochem. Soc.* **2002**, *149*, E252.
- [19] a) Z. Y. Liu, T. Duchon, H. R. Wang, D. C. Grinter, I. Waluyo, J. Zhou, Q. Liu, B. Jeong, E. J. Crumlin, V. Matolin, D. J. Stacchiola, J. A. Rodriguez, S. D. Senanayake, *Phys. Chem. Chem. Phys.* **2016**, *18*, 16621; b) M. Z. Ouyang, P. Boldrin, R. C. Maher, X. L. Chen, X. H. Liu, L. F. Cohen, N. P. Brandon, *Appl. Catal., B.* **2019**, *248*, 332.
- [20] a) N. Laosiripojana, S. Assabumrungrat, *Appl. Catal., B.* **2005**, *60*, 107; b) J. Cortes, E. Valencia, P. Araya, *Catal. Lett.* **2006**, *112*, 121; c) Z. C. Liu, G. Z. Lu, Y. Guo, Y. Q. Wang, Y. L. Guo, *Catal. Sci. Technol.* **2011**, *1*, 1006.
- [21] D. Plecher, R. Greff, R. Peat, L. M. Peter, J. Robinson, *Instrumental Methods in Electrochemistry*, Ellis Woodhead publishing, Cambridge, England **2001**.
- [22] a) Z. Y. Liu, D. C. Grinter, P. G. Lustemberg, T. D. Nguyen-Phan, Y. H. Zhou, S. Luo, I. Waluyo, E. J. Crumlin, D. J. Stacchiola, J. Zhou, J. Carrasco, H. F. Busnengo, M. V. Ganduglia-Pirovano, S. D. Senanayake, J. A. Rodriguez, *Angew. Chem., Int. Ed.* **2016**, *55*, 7455; b) P. G. Lustemberg, P. J. Ramirez, Z. Y. Liu, R. A. Gutierrez, D. G. Grinter, J. Carrasco, S. D. Senanayake, J. A. Rodriguez, M. V. Ganduglia-Pirovano, *ACS Catal.* **2016**, *6*, 8184; c) P. G. Lustemberg, R. M. Palomino, R. A. Gutierrez, D. C. Grinter, M. Vorokhta, Z. Y. Liu, P. J. Ramirez, V. Matolin, M. V. Ganduglia-Pirovano, S. D. Senanayake, J. A. Rodriguez, *J. Am. Chem. Soc.* **2018**, *140*, 7681.

- [23] a) S. D. Senanayake, D. Stacchiola, J. Evans, M. Estrella, L. Barrio, M. Perez, J. Hrbek, J. A. Rodriguez, *J. Catal.* **2010**, 271, 392; b) T. Staudt, Y. Lykhach, N. Tsud, T. Skala, K. C. Prince, V. Matolin, J. Libuda, *J. Phys. Chem. C* **2011**, 115, 8716.
- [24] K. Mudiyansele, S. D. Senanayake, L. Fera, S. Kundu, A. E. Baber, J. Graciani, A. B. Vidal, S. Agnoli, J. Evans, R. Chang, S. Axnanda, Z. Liu, J. F. Sanz, P. Liu, J. A. Rodriguez, D. J. Stacchiola, *Angew. Chem., Int. Ed.* **2013**, 52, 5101.
- [25] a) L. L. Patera, C. Africh, R. S. Weatherup, R. Blume, S. Bhardwaj, C. Castellarin-Cudia, A. Knop-Gericke, R. Schloegl, G. Comelli, S. Hofmann, C. Cepek, *ACS Nano* **2013**, 7, 7901; b) Z. Liu, T. Duchon, H. Wang, E. W. Peterson, Y. Zhou, S. Luo, V. Matolin, D. J. Stacchiola, J. A. Rodriguez, S. D. Senanayake, *J. Phys. Chem. C* **2015**, 119, 18248.
- [26] M. Baron, O. Bondarchuk, D. Stacchiola, S. Shaikhutdinov, H. J. Freund, *J. Phys. Chem. C* **2009**, 113, 6042.
- [27] Z. L. A. Feng, C. B. Gopal, X. F. Ye, Z. X. Guan, B. Jeong, E. Crumlin, W. C. Chueh, *Chem. Mater.* **2016**, 28, 6233.
- [28] W. C. Chueh, A. H. McDaniel, M. E. Grass, Y. Hao, N. Jabeen, Z. Liu, S. M. Haile, K. F. McCarty, H. Bluhm, F. El Gabaly, *Chem. Mater.* **2012**, 24, 1876.
- [29] G. Liu, Z. Hao, X. Mi, N. Ma, H. Zhang, Y. Li, S. Zhan, *Front. Environ. Chem.* **2021**, 2, 672844.
- [30] a) H. Ha, S. Yoon, K. An, H. Y. Kim, *ACS Catal.* **2018**, 8, 11491; b) S. Yoon, H. Ha, J. Kim, E. Nam, M. Yoo, B. Jeong, H. Y. Kim, K. An, *J. Mater. Chem. A* **2021**, 9, 26381.
- [31] M. Yoo, Y.-S. Yu, H. Ha, S. Lee, J.-S. Choi, S. Oh, E. Kang, H. Choi, H. An, K.-S. Lee, *Energy Environ. Sci.* **2020**, 13, 1231.
- [32] W. Jung, K. L. Gu, Y. Choi, S. M. Haile, *Energy Environ. Sci.* **2014**, 7, 1685.
- [33] G. Kresse, J. Furthmuller, *Comput. Mater. Sci.* **1996**, 6, 15.
- [34] J. P. Perdew, K. Burke, M. Ernzerhof, *Phys. Rev. Lett.* **1996**, 77, 3865.
- [35] P. E. Blochl, *Phys. Rev. B* **1994**, 50, 17953.
- [36] S. L. Dudarev, G. A. Botton, S. Y. Savrasov, C. J. Humphreys, A. P. Sutton, *Phys. Rev. B* **1998**, 57, 1505.
- [37] H. Y. Kim, G. Henkelman, *J. Phys. Chem. Lett.* **2013**, 4, 216.
- [38] G. Henkelman, B. P. Uberuaga, H. Jónsson, *J. Chem. Phys.* **2000**, 113, 9901.